Extreme events in frequency-swept semiconductor lasers

A. Stroganov, A. V. Kovalev, and E. A. Viktorov*
Institute of Advanced Data Transfer Systems, ITMO University, Saint Petersburg 199034, Russia

(Received 7 April 2024; accepted 1 August 2024; published 30 August 2024)

We analyze a delay differential equation model for a frequency-swept semiconductor laser and demonstrate existence of extreme events in its dynamics, with probabilities heavily dependent on the sweep rate. The extreme events appear even in absence of any noise in the system and do not exhibit significant dependence on its presence. We investigate the problem numerically and show that intensity dynamics of these events are highly localized in the filter detuning space. Overlaying it with the structure of steady-state and periodic solutions of the static system, we show that the dynamics is governed by attraction to these periodic solutions and such extreme events occur as a result of passing through the region of stable high-intensity bridge of periodic solutions.

DOI: 10.1103/PhysRevE.110.024220

I. INTRODUCTION

The study of rare and extreme events (EEs), in certain cases referred to as rogue waves, is an actively explored interdisciplinary research field, and their investigation is considered to be of great importance as these events are hard to predict, while their appearance may cause abnormalities, functional failures in models or devices, or lead to severe consequences in areas such as geology, climatology, population dynamics, or economics [1–4].

In EE analysis, definitions may vary depending on the system under investigation. Nonetheless, they are all aimed at capturing the main features of extreme events, which are their low occurrence rate and high deviation of their amplitude from the average that can be related to presence of a long tail in the overall statistical distribution. There are several widely used criteria, typically defining event amplitude thresholds based on certain deviation from the mean of population (expressed in a specific number of standard deviations [5–7]) or referenced to a value called abnormality index (AI) [8–10]. Alternatively, or often as a complementary step, analysis of intensity distributions may be performed to indicate presence of an extended or heavy tail and its deviation from the expected distribution [11–13].

In the optical domain, extreme events or optical rogue waves were observed and investigated in a variety of systems, including mode-locked lasers [14,15], semiconductor lasers with continuous-wave [7,16] or chaotic [17] optical injection, external cavity [5,18], phase-conjugated feedback [10,19], broad-area VCSELs [12,20,21], nonlinear optical fibers, and other optical systems [9,22,23].

A number of recent works develop approaches to prediction of extreme events using machine learning, reservoir computing and other advanced computational and forecasting techniques [24,25]. Nevertheless, the majority of studies are still limited to identification of presence of extreme events and analysis of their statistics, without going deeper into their possible origins.

In our work, we investigate the appearance of extreme events in a frequency-swept semiconductor laser with a narrow-band intracavity filter. Frequency-swept lasers are widely explored and used in the context of optical coherence tomography (OCT) [26,27], light detection and ranging (LiDAR) [28,29], and other applications [30,31]. It has been previously shown that semiconductor lasers may have complex asymmetric steady-state and periodic solutions and exhibit nonlinear behavior [32]. Due to this asymmetric structure and induced nonlinearity, the system exhibits different behavior for different frequency detuning directions: we have previously shown a stable periodic dynamics and subharmonic locking effects for positive detunings in a wide range of sweep rates [33], and now focus on the opposite (negative) sweep direction. In this work, we demonstrate the appearance of extreme events introduced by the frequency sweep, and analyze their origin, structure and statistics with respect to the bifurcation structure of periodic solutions and the sweep rate.

II. MODEL

In our study, we work with a ring cavity laser model, considering unidirectional generation and presence of a narrow-band intracavity spectral filter, and employ the same approach as in a number of preceding works [32–34]. We start with a set of equations governing the complex electrical field amplitude $\tilde{E}$ and time-dependent cumulative saturable gain G as

$$\gamma^{-1}\frac{d\tilde{E}}{dt} + (1 + i\Delta)\tilde{E} = \sqrt{\kappa}e^{\frac{1-i\alpha}{2}G}\tilde{E}(t-1), \tag{1}$$

$$\eta^{-1}\frac{dG}{dt} = J - G - (e^{G} - 1)|\tilde{E}(t-1)|^2, \tag{2}$$

where the whole model is normalized to the cavity round trip time. The normalization-related multipliers γ and η correspond to the bandwidth of the intracavity spectral filter multiplied by the cavity round trip time, and to the ratio of the cavity round trip time and the carrier density relaxation time, respectively. Linear intensity losses per round trip are described by the attenuation factor κ, the pump parameter is denoted by J, and α is the linewidth enhancement factor. The frequency sweep is introduced by the parameter $\Delta = \Delta(t)$, which defines the detuning with respect to a reference laser cavity mode frequency.

*Contact author: eaviktorov@itmo.ru

TABLE I. Parameters used in the model.

Parameter	Value
Attenuation factor (κ)	0.35
Linewidth enhancement factor (α)	5
Pump parameter (J)	10
Filter bandwidth * round trip time (γ)	0.25
Ratio of cavity round trip time and carrier density relaxation time (η)	1

With a substitution $\tilde{E} = Ee^{-i\int_0^t \Delta(x)dx}$, these equations may be transformed into

$$\gamma^{-1}\frac{dE}{dt} + E = \sqrt{\kappa}e^{\frac{1-i\alpha}{2}G-i\phi(t)}E(t-1), \tag{3}$$

$$\eta^{-1}\frac{dG}{dt} = J - G - (e^G - 1)|E(t-1)|^2, \tag{4}$$

where $\phi(t) = \int_{t-1}^t \Delta(x)dx$ represents accumulated filter detuning. In our further analysis, we consider linear detuning sweep, such that it can be described as $\phi(t) = \phi(0) + \epsilon t$, where ϵ is the frequency sweep rate. For simplicity, we later on assume $\phi(0) = 0$. Other fixed parameter values used in the model are the same as in our previous work [33], as it helps to complement the analysis done before, and they can be seen in Table I.

It should be noted that Eqs. (3)–(4) and their obtained solutions are 2π periodic with respect to the filter detuning and will be the same for $\phi \to \phi + 2\pi n$, where n is an integer number. To obtain and analyze CW and periodic branches of a static system (in absence of the filter sweep $\epsilon = 0$, so that the system is autonomous), we use DDE-BIFTOOL [35] considering a phase parameter $\phi(t) = \phi_0$.

The bifurcation structure for the static laser system investigated in this work can be seen in Fig. 1: it contains stable and unstable steady states (corresponding to the cavity modes) with two fold and a number of Hopf bifurcation points. The steady states are connected by the bridge of periodic solutions with multiple folds and branches. This complicated structure is defined by the narrow-band filtering in the cavity and the presence of the phase-amplitude coupling in the semiconductor gain medium leading to the nonlinear cavity behavior [32]. Disconnected branch of periodic solutions, or isola, is also shown in Fig. 1(c) in more detail to illustrate the complexity of folds and coexisting branches of stable and unstable limit cycles. Even though not required for understanding of this work, the extended version of the isola solutions with secondary branches of period doubling solutions can also be seen in the Appendix. We note that the loci of folds are very close to the loci of the period doubling solutions, for which we only show solutions that have stable regions. There are three loci of the stable periodic solutions, which are important for the further analysis. They are indicated in Fig. 1 as top bridge (TB), bottom bridge (BB) and isola solutions. It is important to note for further analysis that 2π periodicity of the solutions and the fold over cause the BB of a given branch to be under the TB of the adjacent branch. This specific bistability between stable periodic solutions with very different amplitudes is indicated later in Fig. 5. More detailed descriptions and analysis of the steady-state, bifurcation points, bridge, and isola solutions for this system can be found in Ref. [33], while here we limit the details to the extent required within the context of this study.

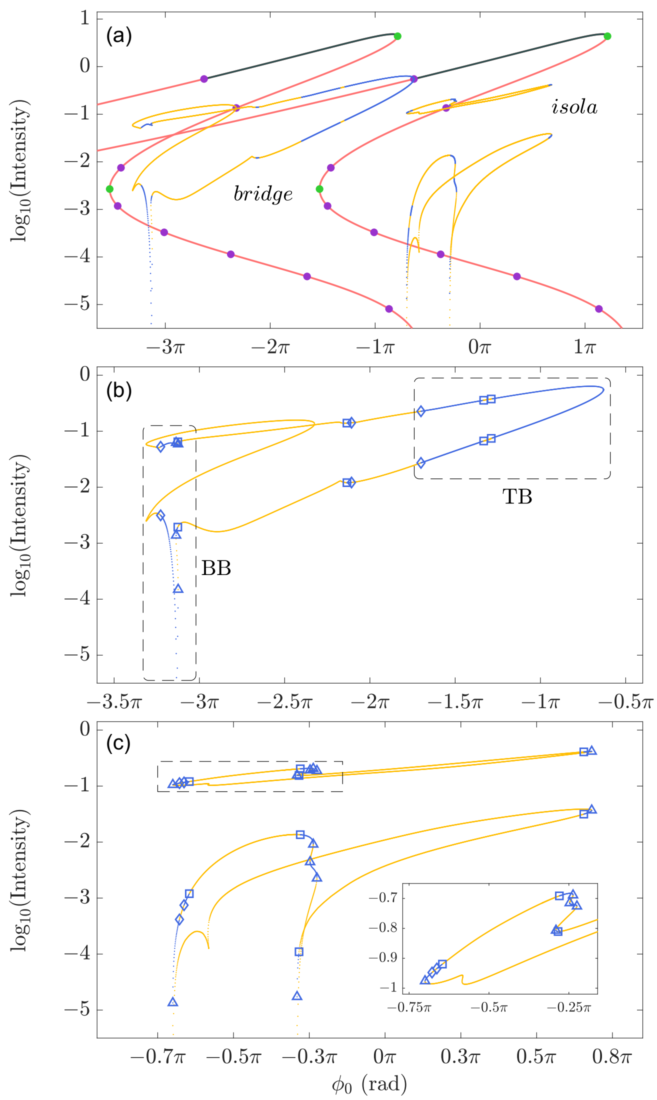

FIG. 1. The logarithm of intensity (a) of two CW branches and extrema of periodic bridge and isola solutions for static $\phi = \phi_0$. Black (red) lines correspond to stable (unstable) steady-state solutions in absence of any sweep ($\epsilon = 0$). Green and purple circles indicate fold and Hopf bifurcation points. Stable (unstable) branches of the periodic solutions are represented by blue (yellow) lines. The solutions and all corresponding bifurcation points are 2π periodic with respect to ϕ; for simplicity, only two CW branches together with one of each type of periodic branches are shown. (b) provides details of the bridge solutions, with indication of top (TB) and bottom (BB) parts. The points of the stable region bifurcations are denoted by triangles (fold), squares (period doubling), and diamonds (torus). (c) provides details of isola solutions, with the inset showing the folded region.

III. GENERAL DYNAMICS AND CRITERIA

To obtain the first understanding of the system's dynamics in the negative sweep direction (going from right to left along parameter ϕ through the structure of CW and periodic

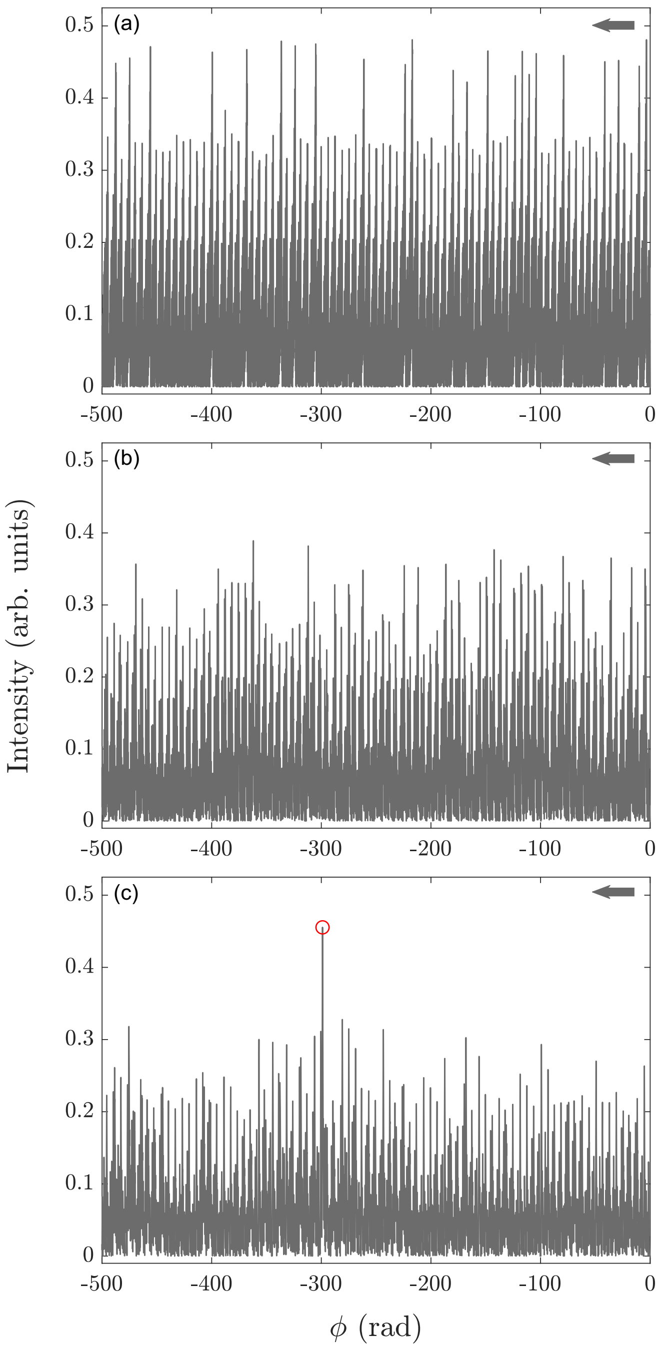

FIG. 2. Time traces for various sweep rates ϵ values: (a)$\epsilon = -0.05$, (b)$\epsilon = -0.20$, and (c)$\epsilon = -0.35$. The time axis is referenced to filter detuning parameter $\phi = \epsilon t$. The arrows indicate that the traces should be read from right to left due to the negative ϵ values. The red circle in (c) denotes the extreme event according to the definition $I_{\mathrm{EE}} \geqslant \mu + 5\sigma$.

solutions described before), we investigate the time traces for various sweep rates: they can be seen in Fig. 2. The minus sign in the value of ϵ indicates the negative sweep direction. It should be noted that these traces should be read from right to left, as $\phi = \epsilon * t$ and ϵ is negative—this is indicated by the arrows in the corresponding plots and later in this work. For all the illustrated cases there is a high number of events, with some of them not even being distinguishable in the plots due to their high density, especially those with smaller intensities. An event is being defined as an intensity peak (local maximum) in the recorded time trace, while the event amplitude is the value of the corresponding intensity peak $I_{\mathrm{EE}} = \max|\mathrm{E}|^2$. The plots for various sweep rates clearly have different visual appearance, and low-probability events with outstandingly high intensities, which can be seen, for example, in cases of $\epsilon = 0.05$ [Fig. 2(a)] or $\epsilon = 0.35$ [Fig. 2(c)].

Definitions of extreme events may vary: in oceanographic studies the criterion is usually taken as abnormality index $\mathrm{AI} = 2 \equiv \mathrm{H}_{\mathrm{RW}} \geqslant 2\mathrm{H}_{\mathrm{s}}$, which means that a wave height should exceed the value called significant wave height H_{s} (the average of one-third of the highest waves) by a factor of 2 to be qualified as a rogue wave. Alternatively, as statistical properties of the wave heights distribution in such systems lead to $H_s \approx 4\sigma$, it is often substituted with $\mu + 8\sigma$, defined on mean (μ) and standard deviation (σ) of the recorded data [36,37]. Nevertheless, in the domains of optics and laser physics, the observable variables and statistical properties of the system may differ considerably—this adds complexity to the choice of appropriate criteria, with no full consensus reached in the community so far. While abnormality index remains valid and widely used, on many occasions it may appear too soft to isolate the events with typical features of extreme events. The alternative criterion based on mean and standard deviation varies considerably from work to work (typically $4\sigma - 8\sigma$) and may be applied on the full recorded data or on the population of events' intensities [7,12,16,18,38,39].

In our work, we consider the criterion based on mean and five times standard deviations of the events population, such that $I_{\mathrm{EE}} \geqslant \mu_{\mathrm{events}} + 5\sigma_{\mathrm{events}}$: for our system $H_s \approx 2.5\sigma_{\mathrm{events}}$ within the whole range of investigated sweep rates. As such, we consider the criterion based on 5σ to be reasonable, and its implementation allows us to well isolate the high-intensity peaks of interest. It should be admitted that, as in any other work related to extreme events, the choice of other criteria may identify more or less events as extreme, while the effect of the corresponding change in the threshold value definition may often be counterbalanced by a change in the system parameters (for example by changing the value of the pump parameter). The criterion based on abnormality index $\mathrm{AI} = 2$ gives lower estimations of the EE threshold in our case and does not allow to clearly isolate the events of interest. Nevertheless, we still indicate its value in some figures to clearly show its position. As was noted before, the sweep rates affect the dynamics and intensity distribution of events in investigated time traces, so in our analysis the threshold value for extreme events (excess of it qualifies the event as extreme) is calculated for each individual fixed value of the sweep rate ϵ.

The intensities of individual events within traces, such as those seen in Fig. 2, may be systematically assessed for a range of different sweep rates ϵ to make a scatter plot in Fig. 3(a) with the sweep rate on the horizontal axis and detected events' intensity on the vertical axis: in each column there are blue dots reflecting all the events observed within the time trace for corresponding ϵ. It can be seen that maximum intensities of events in corresponding dynamics vary quite considerably in a nonmonotonic manner with the value of ϵ, which supports the initial observation from Fig. 2. The levels of the mean, median, and five standard deviation values of events' population for each given sweep rate, as well as calculated threshold values (indicated by red bars at the top) to

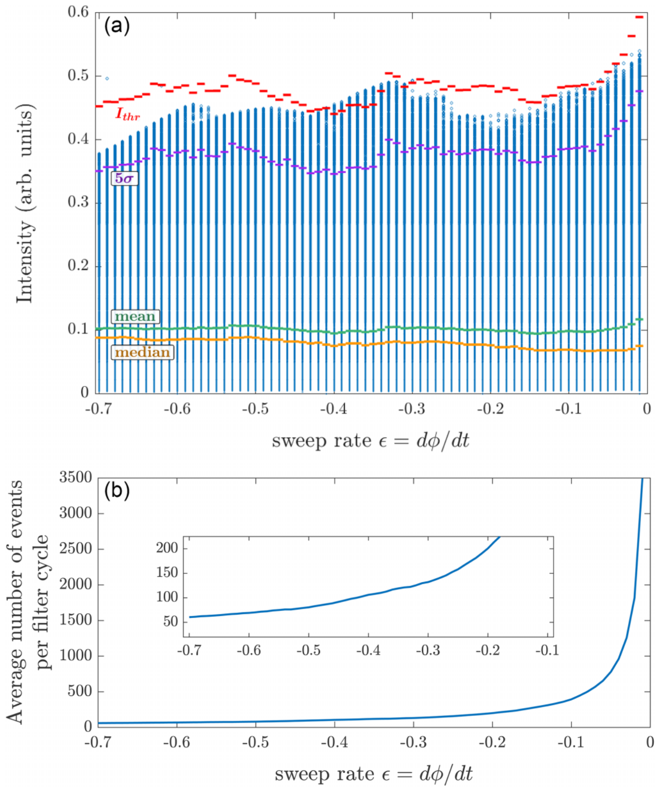

FIG. 3. Individual intensities of all detected events plotted as a scatter (blue circles) for a range of (a)$\epsilon = [-0.7, 0]$. The plot also contains the lines corresponding to mean (green), median (orange), and 5σ (purple) values of events' intensities for a given sweep rate. The red bars indicate calculated threshold intensities to qualify for extreme events: $I_{\rm thr} = \text{mean} + 5\sigma$. (b) shows average number of events per filter cycle (while detuning parameter ϕ is swept within 2π) for sweep rates ϵ from the same range.

qualify the events as extreme, complement this plot such that it gives all the information needed for analysis and identification of EEs.

The blue dots above the EE threshold bar indicate that there are extreme events observed for corresponding sweep rate values: this is the case for $\epsilon = [-0.30, -0.41]$. It should be emphasized again that the threshold values within the same criterion are calculated separately for the time traces obtained at each given sweep rate and may vary depending on the latter: this approach was previously used in other works where the variable parameter introduces considerable change in the overall dynamics [5]. The purple line related to the value of 5σ indicates that the variation of the EE threshold intensity level is primarily linked to the change in the standard deviation value, while the mean and median experience only gradual changes within the range of sweep rates.

As has been noted before, the Eqs. (3)–(4) are 2π periodic with respect to the filter detuning parameter ϕ, so for description of periodic passage of the filter through the system's bifurcation structure we define a filter cycle as a change of filter detuning ϕ by 2π: in case the cumulative detuning accounts for $2\pi n$ change, where n is an integer number, we say that the filter passed n cycles. As such, the number of events per filter cycle can also be assessed [Fig. 3(b)]: it experiences a smooth decay with a rather steep change for $\epsilon = (-0.0, -0.1]$, followed by a more gradual decline for faster sweep rates.

It should also be specifically emphasized that no noise has been included in the model at this stage, so extreme events can be attributed to the presence of the sweep in the system, which results in forcing the trajectory to slowly pass through the bifurcation structure defined in the static case—this will be discussed in more detail further below. Appearance of extreme events in laser systems where some parameters are being swept has been shown before for current modulation [39,40].

As a next step of our analysis, the probability of EE is obtained [Fig. 4(a)]: for its calculation, time traces with a length of 100 000 cavity round trips were recorded for different sweep rate values. Longer recordings, tested for individual traces, do not give any considerable deviations from the obtained values. The EE criterion was recalculated for each sweep rate parameter ϵ and the probability of EE was assessed with respect to the total number of events as $P_{\rm EE} = N_{\rm EE}/N_{\rm events}$, where $N_{\rm EE}$ and $N_{\rm events}$ are number of extreme events and a total number of events, respectively. The assessment was performed both for cases without noise and with artificially added random phase and intensity noise. The noise was introduced as an additive Gaussian source in Eq. (3), having a standard deviation of 0.001. Plotting EE probability as a function of the sweep rate $P(\epsilon)$, a sharp peak is observed in a rather narrow range of sweep rate values region $\epsilon = [-0.30, -0.41]$ as expected based on Fig. 3. It is important to note that there is no significant difference between the two cases, which confirms that observed EEs do not originate from the noise and random fluctuations in the system, but from the presence of the frequency filter sweep. This differs from the typical situations, when EEs are primarily caused by various noise in the system close to bistability regions [41,42] or may be enhanced or suppressed by it [43]. The bottom panels of Figs. 4(b)–4(d) show probability density function (PDF) distributions for events' intensities at three different sweep rates: $\epsilon = -0.30$ [right side of the interval shown in Fig. 4(a) with relatively limited number of EEs identified], $\epsilon = -0.36$ (middle of the range with the highest EE probability), and $\epsilon = -0.42$ (left side of the interval with no EEs identified). Besides, two vertical dashed lines correspond to the threshold values to qualify extreme events for AI = 2 (blue) and $I_{\rm thr} = \text{mean} + 5\sigma$ (orange) criteria: it can be seen that AI criterion is always softer and events identified by it do not clearly exhibit the typical features of extreme events—they do not come from a tail deviating from the expected distribution, nor are relatively rare in occurrence. The second criterion appears to be more adequate, as it highlights presence of events from the deviating tails and does not identify EEs in absence of such deviations. While it may not exactly catch all the events deviating from the expected statistics, this is also rarely achieved with any other criterion. Importantly, all identified events comply with the definition of EE and we analyze those further below and show their distinct features and dynamics.

To investigate the EE dynamics for these sweep rates, an overlay with the CW and periodic solutions of the static system can be done. The time traces for $\epsilon = -0.36$ have been chosen for this and further analysis steps as this value

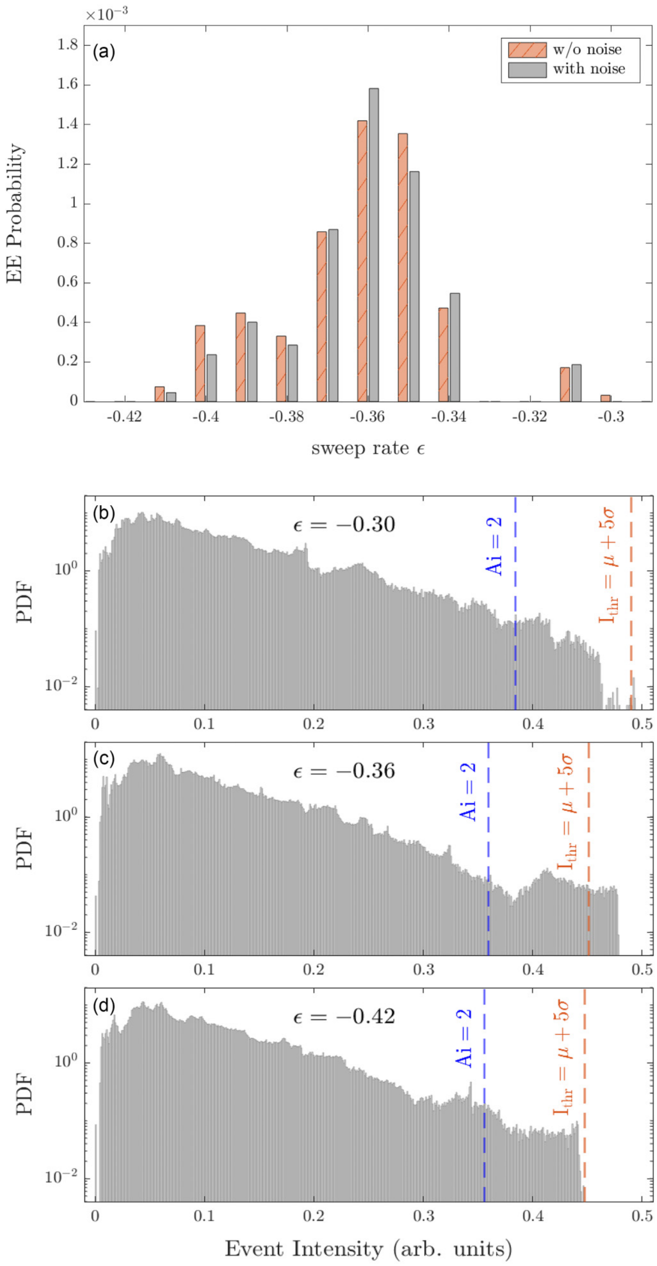

FIG. 4. Top panel (a): Probability of extreme events vs sweep rate for $\epsilon = [-0.28, -0.43]$ range. Two cases are illustrated: system as is (orange patterned bars) and with added noise (gray bars). Bottom panels (b)–(d): PDF histograms of events' intensities for $\epsilon = -0.30$, $\epsilon = -0.36$, and $\epsilon = -0.42$ corresponding to the different parts of the range from the top panel. Vertical lines indicate threshold values as defined by two criteria.

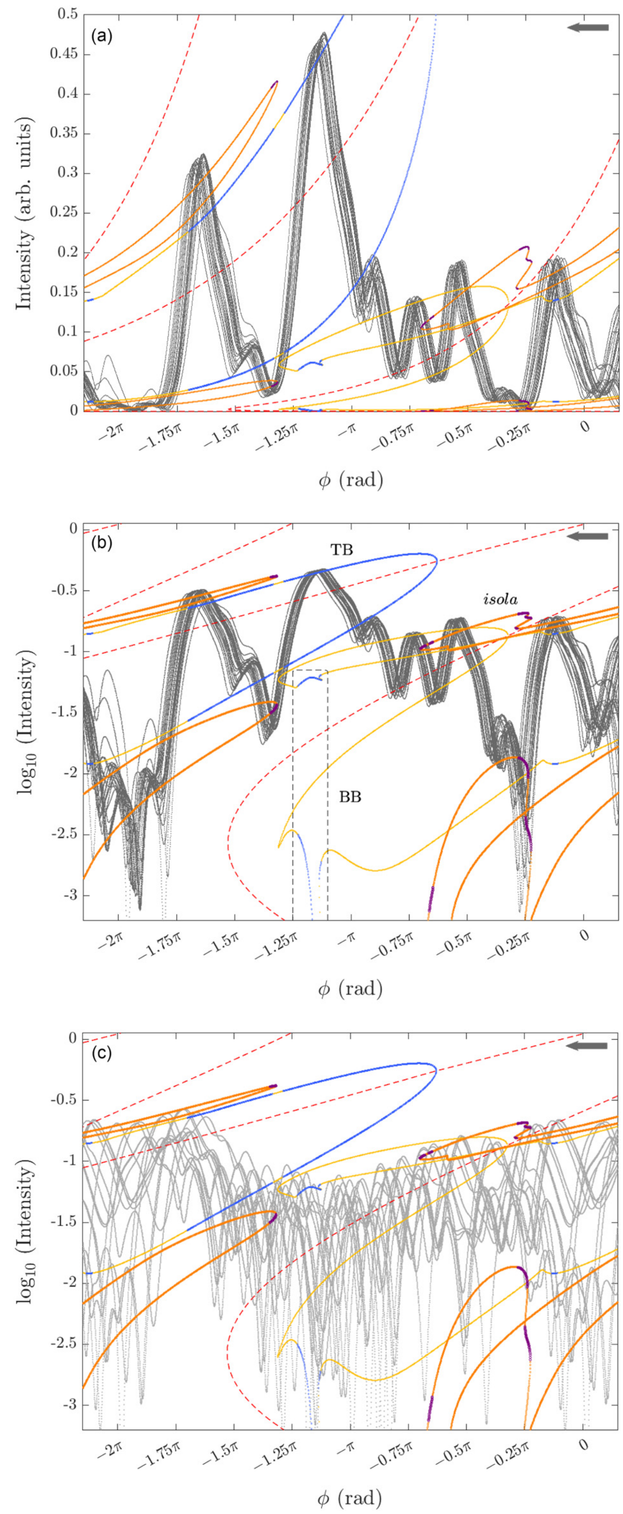

FIG. 5. Examples of (a) 25 intensity trajectories of various EEs and (b) their logarithms for $\epsilon = -0.36$ case plotted by solid dark gray lines. Trajectories' logarithms for 15 non-EE cases are shown in (c). The traces should be read from right to left as denoted by the arrow due to the negative sweep direction. Other notations are as in Fig. 1: red dashed lines correspond to unstable state-state solutions, blue (yellow) lines to the extrema intensity of stable (unstable) regions of bridge solutions, and purple (orange) lines to the extrema intensity of stable (unstable) regions of isola. Note the bistability between TB and BB branches of stable periodic solutions.

corresponds to the highest probability of EE occurrence, therefore requiring less computing power and time to acquire reasonable number of event for statistics. Visualization of these traces can be seen in Fig. 5: it can be noted from Figs. 5(a)–5(b) that traces of all EEs follow almost identical trajectory, except for having small phase shifts with respect to each other. It should be noted once again that these figures should be read from right to left due to the negative filter detuning direction.

The extreme events (which in this case have to exceed threshold value $I_{\text{EE}} \geqslant I_{\text{thr}} \approx 0.4515$) appear in a single well-localized range of detunings in between $-\pi$ and -1.25π as a visit of the stable part of the bridge of periodic solutions indicated by the blue color in the figure. This also implies that their maximum intensity is bound by the corresponding bridge solution intensity. Extreme events may be followed by a secondary (or even higher-order, depending on the sweep rate) peaks, which are always of smaller intensity due to the structure of the bridge and do not qualify as EE according to the defined threshold intensity. It should be noted that trajectories for the gain value G in case of EE also exhibit the same high degree of localization and similarity to each other. In filter detuning cycles where EEs are not present, the trajectories do not exhibit high localization, and do not visit this high-intensity stable part of the bridge, drifting along lower intensity branches [see Fig. 5(c)]. In such non-EE case, the trajectory is also being attracted by the small low-intensity stable bridge region, preventing any occasional deviations and returns to the high-intensity part. To better illustrate these two scenarios, we complement Fig. 5 with Supplemental Material showing the movement of the trajectories in ϕ-intensity-G phase space [44]. In general, overall dynamics of intensity is governed by an itinerary of a complex set of various periodic attractors. Importantly, in our case the behavior of trajectories can be well described by attractors of the static system ($\epsilon = 0$), unlike other works with system parameter sweeps (e.g., pump modulation), where EEs result from the switches between the attractors generated by modulation [42].

First, the trajectory passes the isola, being attracted by one or another stable limit cycles. After the isola, the trajectory goes in one of the two ways, being attracted to one of the two loci of the stable periodic solutions on the bridge. The attraction to the top branch of the bridge (TB) results in EEs with nearly identical well-formed pulse profiles, while the attraction to the stable periodic solution at the bottom branch of the bridge (BB) produces events of much smaller amplitudes without specific shape. The random selection between the two ways is justified by the statistical analysis, but is not depended on noise: it results from high complexity of periodic orbit manifolds of the system, including stable and saddle orbits. This also clearly demonstrates the existing difference between the typical median events and extreme events, which exhibit distinct dynamics in phase space.

As a last step, we analyze the time intervals between the EEs: a histogram representing statistics for the same $\epsilon = -0.36$ case is provided in Fig. 6. The time intervals are expressed in the units of filter cycles (filter detunings of 2π) and recorded occurrences of corresponding time intervals between consequent EEs are counted. This approach is chosen as we previously noted that EEs appear only in a highly localized range of detunings within a filter cycle and have high degree of localization with respect to each other. As can be seen from Fig. 6(a), which represents a histogram with integer binning, the recorded intervals range from 2 to above 350 with a fast decay in occurrence rate. For increased visibility, the same data are plotted as PDF in logarithmic scale in Fig. 6(b), with slightly more coarse binning and two lines indicating a good match with exponential and stretched-exponential (with stretching exponent $\beta = 0.98$ shown for comparison) fits [45],

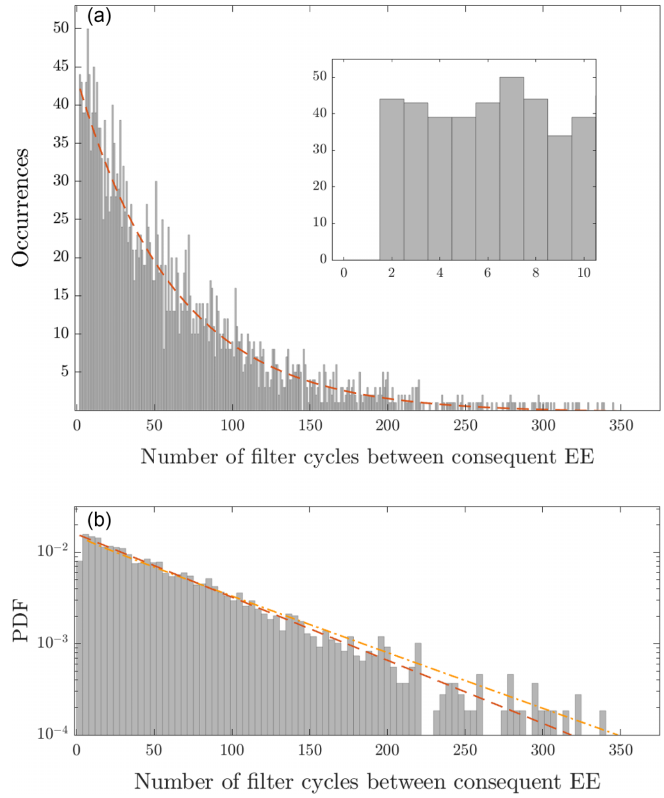

FIG. 6. (a) Histogram with integer binning showing statistics for delay between two consequent EEs in units of filter detuning cycles. The inset shows a zoom-in view at the left part of the histogram: there are no EEs within the same or in consequent filter cycles, which would correspond to the bins with a value of 0 and 1, respectively. (b) PDF representation of the same data in logarithmic scale. More coarse binning is used and lines corresponding to exponential (orange dashed) and stretched-exponential (yellow dash-dotted) fits are shown.

which is in line with observations in [5,20]. The inset in the figure shows the zoom-in version of the left part of the histogram with integer binning: it is important to note that bins with 0 (several EEs within the same filter cycle) and 1 (EEs in consequent filter cycles) are empty. While the former can be justified by the intensity limitations implied by the bridge that we discussed before, we attribute the latter fact to the deep dive of the intensity that is present in every trajectory after EE peaks: EE peak intensities deplete the gain, leading to a fast and deep drop in intensity down to -3 dB or lower in $[-1.8\pi, -2\pi]$ detuning range, which can be clearly seen in logarithmic scale in Fig. 5(b). This puts the trajectory too far from any attractors, which form the EE dynamics, and, taking into account the sweep rate, there is not enough time for the trajectory to reach them before or within the next cycle. It also can be seen from the same figure that there is no such characteristic dip before EEs (on the right from $\phi = 0$).

IV. CONCLUSION

We demonstrate, analyze and explain the appearance of extreme events in a delay differential equation model for a frequency-swept semiconductor laser system with a narrow-band filter. A strongly asymmetric fold over of the continuous wave solution in our system allows coexistence of multiple bifurcation branches and the sweep-induced hopping effects between them. We analyze the identified events and show that they appear in a narrow range of sweep rates and their probability is highly dependent on this parameter. We also show that they appear in absence of any noise in the system and are robust to its addition. The bifurcation structure of the static system is characterized by multiple folding branches, including the bridge and isola of the periodic solutions, which appearance is attributed to the phase-amplitude coupling in the semiconductor gain medium and the narrow-band filtering. In this structure, we identify three key contributing loci of the stable solutions that form a scenario for extreme events in the frequency-swept system with the negative frequency filter detuning sweep via random choice of the trajectory passage itinerary from isola to either top (large amplitude periodic solutions) or bottom (small amplitude periodic solutions) bridge region.

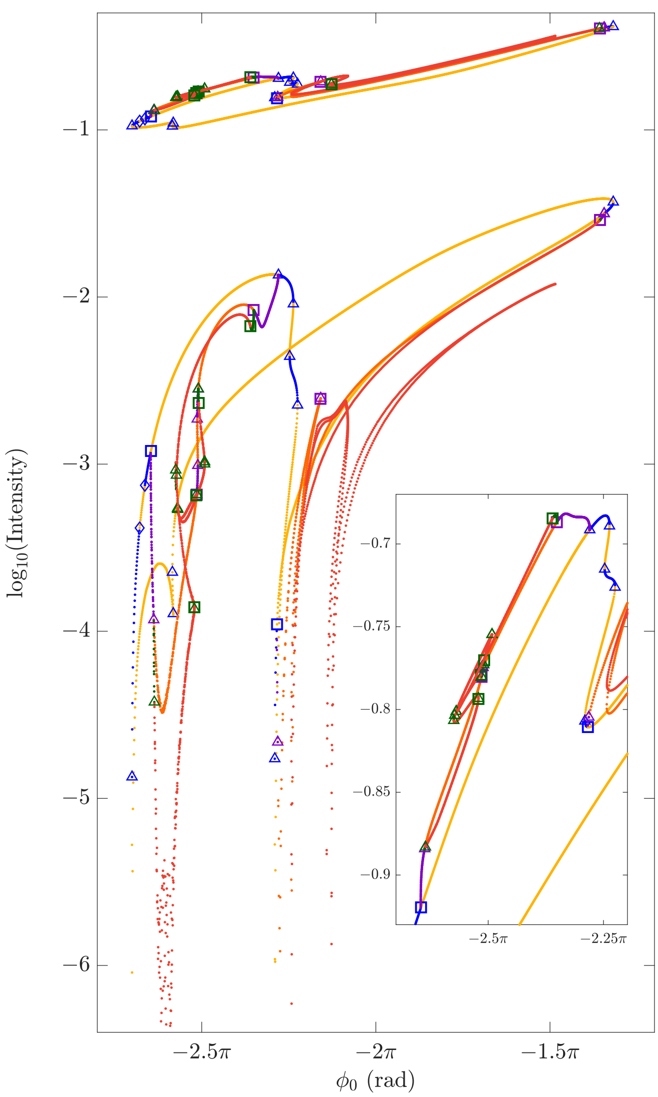

FIG. 7. The extended view of the periodic isola solutions: logarithm of intensity extrema of periodic isola solutions for static $\phi = \phi_0$, including primary solutions, bifurcation points, secondary and tertiary period-doubling branches. Primary stable (unstable) regions are represented by blue (yellow) lines. Secondary branches born from period-doubling bifurcations are denoted by purple (orange) lines for stable (unstable) regions, while tertiary stable (unstable regions) by green (red orange). The points of the stable region bifurcations are denoted by triangles (fold), squares (period doubling), and diamonds (torus), while colors indicate which stable branch the bifurcation point belongs to.

ACKNOWLEDGMENTS

The work of A.V.K. and E.A.V. was supported by the Ministry of Science and Higher Education of the Russian Federation, research Project No. 2019-1442 (Project reference No. FSER-2020-0013).

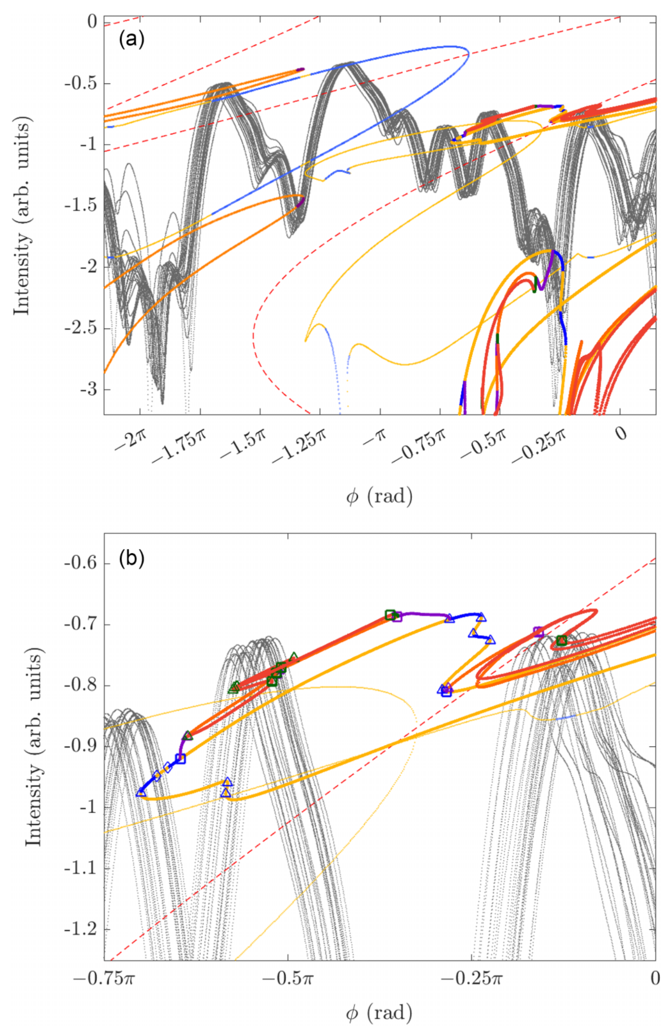

FIG. 8. (a) Overlay of intensity logarithm trajectories with CW and periodic solutions of the static system, illustrating 25 trajectories for various EEs ($\epsilon = -0.36$ case) plotted by solid dark gray lines, and (b) zoom-in on the extended isola region, where trajectories pass through or along it. Trajectories and notations are preserved from Fig. 5(b) and extended with detailed representation of isola. Notations for the extended isola are as in Fig. 7.

APPENDIX: DETAILED ISOLA OF PERIODIC SOLUTIONS

This section provides more detailed view on the structure of isola solutions. Even though, as outlined in the main text, these details may not be necessary for understanding of the paper and description of the intensity trajectory dynamics, we would like to emphasize the complexity of these solutions.

For this purpose, besides the structures showed in Fig. 1 with the bifurcation points (positions and types), we additionally indicate the secondary and tertiary period-doubling solutions arising from them in Fig. 7. Figure 8(a) shows the EE dynamics [same as Fig. 5(b)] with the detailed isola representation, and Fig. 8(b) is a zoom-in on one of the isola regions, where intensity trajectories pass through or along the secondary isola branches. Scattered short regions of stable solutions of these secondary branches may affect the dynamics, but do not allow to reliably identify their particular roles: this also does not deviate or contradict to the observations, descriptions and statements provided in the main text of the paper.

[1] C. Nicolis and G. Nicolis, Extreme events in multivariate deterministic systems, Phys. Rev. E **85**, 056217 (2012).
[2] T. Schweigler and J. Davidsen, Clustering of extreme and recurrent events in deterministic chaotic systems, Phys. Rev. E **84**, 016202 (2011).
[3] H. E. Roman, R. A. Siliprandi, C. Dose, and M. Porto, Long-time correlations in company profit fluctuations: Presence of extreme events, Phys. Rev. E **80**, 036114 (2009).
[4] R. W. Katz, Statistics of extremes in climate change, Climatic Change **100**, 71 (2010).
[5] J. A. Reinoso, J. Zamora-Munt, and C. Masoller, Extreme intensity pulses in a semiconductor laser with a short external cavity, Phys. Rev. E **87**, 062913 (2013).
[6] C. R. Bonazzola, A. A. Hnilo, M. G. Kovalsky, and J. R. Tredicce, Features of the extreme events observed in an all-solid-state laser with a saturable absorber, Phys. Rev. A **92**, 053816 (2015).
[7] C. Bonatto, M. Feyereisen, S. Barland, M. Giudici, C. Masoller, J. R. Rios Leite, and J. R. Tredicce, Deterministic optical rogue waves, Phys. Rev. Lett. **107**, 053901 (2011).
[8] C. Kharif, E. Pelinovsky, and A. Slunyaev, *Rogue Waves in the Ocean*, Advances in Geophysical and Environmental Mechanics and Mathematics (Springer, Berlin, 2009).
[9] J. M. Dudley, F. Dias, M. Erkintalo, and G. Genty, Instabilities, breathers and rogue waves in optics, Nature Photon. **8**, 755 (2014).
[10] E. Mercier, A. Even, E. Mirisola, D. Wolfersberger, and M. Sciamanna, Numerical study of extreme events in a laser diode with phase-conjugate optical feedback, Phys. Rev. E **91**, 042914 (2015).
[11] J. M. Dudley, G. Genty, and B. J. Eggleton, Harnessing and control of optical rogue waves in supercontinuum generation, Opt. Express **16**, 3644 (2008).
[12] C. Rimoldi, S. Barland, F. Prati, and G. Tissoni, Spatiotemporal extreme events in a laser with a saturable absorber, Phys. Rev. A **95**, 023841 (2017).
[13] Y. Zeng, Y. Huang, P. Zhou, P. Mu, and N. Li, Controlling the likelihood of extreme events in an optically pumped spin-vcsel via chaotic optical injection, Opt. Express **31**, 16178 (2023).
[14] J. M. Soto-Crespo, P. Grelu, and N. Akhmediev, Dissipative rogue waves: Extreme pulses generated by passively mode-locked lasers, Phys. Rev. E **84**, 016604 (2011).
[15] M. G. Kovalsky, A. A. Hnilo, and J. R. Tredicce, Extreme events in the Ti:sapphire laser, Opt. Lett. **36**, 4449 (2011).
[16] S. Ge, C. Liu, Y. Huang, P. Zhou, and N. Li, Enhanced extreme events in three cascade-coupled semiconductor lasers, Opt. Express **32**, 13906 (2024).
[17] Y. Huang, P. Zhou, Y. Zeng, R. Zhang, and N. Li, Evolution of extreme events in a semiconductor laser subject to chaotic optical injection, Phys. Rev. A **105**, 043521 (2022).
[18] D. Choi, M. J. Wishon, J. Barnoud, C. Y. Chang, Y. Bouazizi, A. Locquet, and D. S. Citrin, Low-frequency fluctuations in an external-cavity laser leading to extreme events, Phys. Rev. E **93**, 042216 (2016).
[19] A. K. D. Bosco, D. Wolfersberger, and M. Sciamanna, Extreme events in time-delayed nonlinear optics, Opt. Lett. **38**, 703 (2013).
[20] S. Coulibaly, M. G. Clerc, F. Selmi, and S. Barbay, Extreme events following bifurcation to spatiotemporal chaos in a spatially extended microcavity laser, Phys. Rev. A **95**, 023816 (2017).
[21] C. Rimoldi, M. Eslami, F. Prati, and G. Tissoni, Extreme events in a broad-area semiconductor laser with coherent injection, Phys. Rev. A **105**, 023525 (2022).
[22] D. R. Solli, C. Ropers, P. Koonath, and B. Jalali, Optical rogue waves, Nature (London) **450**, 1054 (2007).
[23] A. Coillet, J. Dudley, G. Genty, L. Larger, and Y. K. Chembo, Optical rogue waves in whispering-gallery-mode resonators, Phys. Rev. A **89**, 013835 (2014).
[24] V. A. Pammi, M. G. Clerc, S. Coulibaly, and S. Barbay, Extreme events prediction from nonlocal partial information in a spatiotemporally chaotic microcavity laser, Phys. Rev. Lett. **130**, 223801 (2023).
[25] T. Wang, H. Zhou, Q. Fang, Y. Han, X. Guo, Y. Zhang, C. Qian, H. Chen, S. Barland, S. Xiang, and G. L. Lippi, Reservoir computing-based advance warning of extreme events, Chaos, Solitons & Fractals **181**, 114673 (2024).
[26] J. F. de Boer, R. Leitgeb, and M. Wojtkowski, Twenty-five years of optical coherence tomography: the paradigm shift in sensitivity and speed provided by fourier domain oct invited, Biomed. Opt. Express **8**, 3248 (2017).
[27] S. Slepneva, B. O'Shaughnessy, B. Kelleher, S. P. Hegarty, A. Vladimirov, H.-C. Lyu, K. Karnowski, M. Wojtkowski, and G. Huyet, Dynamics of a short cavity swept source oct laser, Opt. Express **22**, 18177 (2014).
[28] J. Riemensberger, A. Lukashchuk, M. Karpov, W. Weng, E. Lucas, J. Liu, and T. J. Kippenberg, Massively parallel coherent laser ranging using a soliton microcomb, Nature (London) **581**, 164 (2020).

[29] C. Liu, L. Lu, Y. Guo, X. Li, J. Chen, and L. Zhou, Hybrid integrated frequency-modulated continuous-wave laser with synchronous tuning, J. Lightwave Technol. **40**, 5636 (2022).

[30] Y. Nakazaki and S. Yamashita, Fast and wide tuning range wavelength-swept fiber laser based on dispersion tuning and its application to dynamic fbg sensing, Opt. Express **17**, 8310 (2009).

[31] J. Qin, L. Zhang, W. Xie, R. Cheng, Z. Liu, W. Wei, and Y. Dong, Ultra-long range optical frequency domain reflectometry using a coherence-enhanced highly linear frequency-swept fiber laser source, Opt. Express **27**, 19359 (2019).

[32] A. V. Kovalev, P. S. Dmitriev, A. G. Vladimirov, A. Pimenov, G. Huyet, and E. A. Viktorov, Bifurcation structure of a swept-source laser, Phys. Rev. E **101**, 012212 (2020).

[33] A. Stroganov, A. V. Kovalev, and E. A. Viktorov, Subharmonic locking and frequency combs in frequency-swept semiconductor lasers, Phys. Rev. E **107**, 034208 (2023).

[34] S. Slepneva, B. Kelleher, B. O'Shaughnessy, S. P. Hegarty, A. G. Vladimirov, and G. Huyet, Dynamics of fourier domain mode-locked lasers, Opt. Express **21**, 19240 (2013).

[35] K. Engelborghs, T. Luzyanina, and D. Roose, Numerical bifurcation analysis of delay differential equations using DDE-BIFTOOL, ACM Trans. Math. Softw. **28**, 1 (2002).

[36] I. R. Young, *Stochastic Properties of Ocean Waves* (Elsevier, Amsterdam, 1999), Chap. 3, pp. 25–40.

[37] M. Onorato, S. Residori, U. Bortolozzo, A. Montina, and F. T. Arecchi, Rogue waves and their generating mechanisms in different physical contexts, Phys. Rep. **528**, 47 (2013).

[38] P. Durairaj, S. Kanagaraj, S. Kumarasamy, and K. Rajagopal, Emergence of extreme events in a quasiperiodic oscillator, Phys. Rev. E **107**, L022201 (2023).

[39] S. Perrone, R. Vilaseca, J. Zamora-Munt, and C. Masoller, Controlling the likelihood of rogue waves in an optically injected semiconductor laser via direct current modulation, Phys. Rev. A **89**, 033804 (2014).

[40] M. Zaki and M. Hosseini, Tuning of rogue waves in a semiconductor laser by modulating the injection strength, Optik **186**, 259 (2019).

[41] D. Zhao, Y. Li, Q. Liu, H. Zhang, and Y. Xu, The occurrence mechanisms of extreme events in a class of nonlinear duffing-type systems under random excitations, Chaos **33**, 083109 (2023).

[42] J. S. Suelzer, T. B. Simpson, and N. G. Usechak, Extreme pulses in gain-switched semiconductor lasers, Opt. Lett. **48**, 4237 (2023).

[43] J. Zamora-Munt, B. Garbin, S. Barland, M. Giudici, J. R. Rios Leite, C. Masoller, and J. R. Tredicce, Rogue waves in optically injected lasers: Origin, predictability, and suppression, Phys. Rev. A **87**, 035802 (2013).

[44] See Supplemental Material at http://link.aps.org/supplemental/10.1103/PhysRevE.110.024220 for animations of the trajectories' movement through the structure of steady state and periodic solutions in ϕ-Intensity-G space.

[45] A. Clauset, C. R. Shalizi, and M. E. J. Newman, Power-law distributions in empirical data, SIAM Rev. **51**, 661 (2009).